

# UC Berkeley

## UC Berkeley Previously Published Works

### Title

Metal Bonding with 3d and 6d Orbitals: An EPR and ENDOR Spectroscopic Investigation of  $Ti^{3+}-Al$  and  $Th^{3+}-Al$  Heterobimetallic Complexes

### Permalink

<https://escholarship.org/uc/item/9sq907jz>

### Journal

Inorganic Chemistry, 58(12)

### ISSN

0020-1669

### Authors

Rao, Guodong  
Altman, Alison B  
Brown, Alexandra C  
et al.

### Publication Date

2019-06-17

### DOI

10.1021/acs.inorgchem.9b00720

Peer reviewed

## Metal Bonding with 3d and 6d Orbitals: An EPR and ENDOR Spectroscopic Investigation of $\text{Ti}^{3+}$ –Al and $\text{Th}^{3+}$ –Al Heterobimetallic Complexes

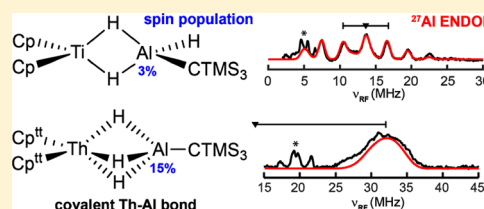
Guodong Rao,<sup>†</sup> Alison B. Altman,<sup>‡</sup> Alexandra C. Brown,<sup>‡</sup> Lizhi Tao,<sup>†</sup> Troy A. Stich,<sup>†,§</sup> John Arnold,<sup>\*,‡</sup> and R. David Britt<sup>\*,†</sup>

<sup>†</sup>Department of Chemistry, University of California at Davis, Davis, California 95616, United States

<sup>‡</sup>Department of Chemistry, University of California at Berkeley, Berkeley, California 94720, United States

### S Supporting Information

**ABSTRACT:** Accessing covalent bonding interactions between actinides and ligating atoms remains a central problem in the field. Our current understanding of actinide bonding is limited because of a paucity of diverse classes of compounds and the lack of established models. We recently synthesized a thorium (Th)–aluminum (Al) heterobimetallic molecule that represents a new class of low-valent Th-containing compounds. To gain further insight into this system and actinide–metal bonding more generally, it is useful to study their underlying electronic structures. Here, we report characterization by electron paramagnetic resonance (EPR) and electron–nuclear double resonance (ENDOR) spectroscopy of two heterobimetallic compounds: (i) a  $\text{Cp}^{\text{tt}}_2\text{ThH}_3\text{AlCTMS}_3$  [TMS =  $\text{Si}(\text{CH}_3)_3$ ;  $\text{Cp}^{\text{tt}}$  = 1,3-di-*tert*-butylcyclopentadienyl] complex with bridging hydrides and (ii) an actinide-free  $\text{Cp}_2\text{TiH}_3\text{AlCTMS}_3$  (Cp = cyclopentadienyl) analogue. Analyses of the hyperfine interactions between the paramagnetic trivalent metal centers and the surrounding magnetic nuclei,  $^1\text{H}$  and  $^{27}\text{Al}$ , yield spin distributions over both complexes. These results show that while the bridging hydrides in the two complexes have similar hyperfine couplings ( $a_{\text{iso}} = -9.7$  and  $-10.7$  MHz, respectively), the spin density on the Al ion in the  $\text{Th}^{3+}$  complex is  $\sim 5$ -fold larger than that in the titanium(3+) ( $\text{Ti}^{3+}$ ) analogue. This suggests a direct orbital overlap between Th and Al, leading to a covalent interaction between Th and Al. Our quantitative investigation by a pulse EPR technique deepens our understanding of actinide bonding to main-group elements.



## INTRODUCTION

The chemistry of actinides is not only of fundamental interest but also of practical importance in nuclear fuel processing and recycling,<sup>1,2</sup> as well as in the expansion of their industrial applications.<sup>3</sup> Their unique properties arise, in part, because of the large radial extension of 5f and 6d orbitals combined with strong spin–orbital couplings and relativistic effects.<sup>4</sup> Owing to the complex interplay between these factors and the small number of differing classes of actinide compounds, it is difficult to predict and model their behavior. Central to these problems is understanding the covalency of bonding—the extent of mixing between the ligand and metal orbitals—that is crucial in describing the electronic structures and thus predicting the chemical properties of actinide compounds.<sup>5,6</sup> Covalent interactions are of particular importance for early actinides because they have large atomic radii that allow both 5f and 6d orbitals to participate in bonding. This results in rich redox chemistry that resembles transition metals, although their larger size and more diffuse orbitals give rise to unique bonding patterns.<sup>5,7–9</sup> To what extent these orbitals engage in covalent bonding remains an active field of study with computational and experimental challenges; however, work with uranium (U) compounds has shown the importance of both sets of orbitals.<sup>10–14</sup>

A variety of spectroscopic methods have been used to directly probe and quantify the covalency in transition-metal complexes, including photoelectron, Mössbauer, ligand K-edge X-ray absorption, and electron paramagnetic resonance (EPR) spectroscopies.<sup>15–17</sup> They have also recently been applied to the f-block elements, providing insights into the covalency of both lanthanide and actinide compounds.<sup>10,14,18–21</sup> For systems containing unpaired electrons, EPR spectroscopy is a particularly useful tool to probe the electronic structure of the molecule. For example, when the first thorium(3+) ( $\text{Th}^{3+}$ ) compound was synthesized, EPR spectroscopy provided the key evidence that the ground-state configuration is  $6d^1$  instead of  $5f^1$ .<sup>22</sup> Moreover, the chemistry of actinide molecules and materials is oftentimes governed by small differences in the ligand environment and covalent interactions, and it remains a challenge to experimentally probe and quantify these subtle but important differences. Pulse EPR techniques are particularly adept at measuring ligand hyperfine interactions (HFIs), which can be used to map the spin distribution and analyze the bonding properties of the molecule.<sup>17</sup> The application of pulse EPR techniques in actinide chemistry was recently demon-

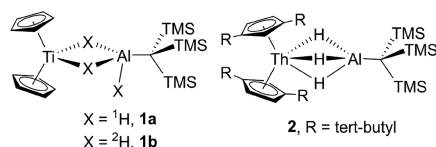
Received: March 12, 2019

Published: June 2, 2019

strated by the pioneering work of Formanuk et al., in which hyperfine sublevel correlation (HYSCORE) spectroscopy was employed to investigate the covalency in a  $(\text{Cp}^{\text{tt}})_3\text{Th}$  ( $\text{Cp}^{\text{tt}} = 1,3\text{-}^i\text{Bu-C}_5\text{H}_3$ ) complex and a  $(\text{Cp}^{\text{tt}})_3\text{U}$  analogue.<sup>23</sup> By measuring the hyperfine couplings from the  $^{13}\text{C}$  and  $^1\text{H}$  nuclei in the aromatic ligands, it was concluded that the spin delocalization onto the  $\text{Cp}^{\text{tt}}$  ligand in the U complex is at least 3 times larger than that in the Th analogue and is caused by a symmetry-driven orbital overlap between the 5f electrons and ligand orbitals. While this demonstrates the power of this technique in elucidating the electronic structure of actinide complexes, it also leaves open the question as to how to contextualize this understanding in terms of the established models developed for transition-metal complexes.

To directly compare the actinide electronic structure with transition-metal behavior, we recently synthesized a new class of  $\text{Th}^{3+}$  complexes containing an anionic aluminum hydride (alanate) ligand, together with a titanium(3+) ( $\text{Ti}^{3+}$ ) analogue (Scheme 1).<sup>24,25</sup> As mentioned above,  $\text{Th}^{3+}$  ions generally

**Scheme 1.**  $\text{M}^{3+}$ –Al Heterobimetallic Complexes Used in This Study



adopt a  $6d^1$  ground-state electronic configuration. Compound **2** is therefore a system well-suited to the use of EPR spectroscopy to directly probe the properties of 6d orbitals and to understand their roles in actinide bonding. The aluminum (Al) ion and bridging hydrides in these molecules possess magnetic nuclei ( $I = 5/2$  for  $^{27}\text{Al}$  and  $1/2$  for  $^1\text{H}$ , respectively) and thereby provide direct probes to quantify covalency. Our previous quantum chemical study implied the presence of a Th–Al bonding interaction.<sup>25</sup> This unique metal–metal interaction suggests that the study of Th–Al bimetallic compounds may inform models of actinide–group 13 interactions that are important in the safe handling of nuclear fuels, as well as provide insight into the synthesis and properties of Th–Al alloys.<sup>26,27</sup>

To gain further and more quantitative insights into the bonding properties, especially the M–Al interaction, in these complexes, we now report thorough EPR and electron–nuclear double resonance (ENDOR) spectroscopic characterizations of these two complexes. The HFIs of the bridging hydrides and Al ions are measured for both the  $\text{Ti}^{3+}$  and  $\text{Th}^{3+}$  complexes. A detailed analysis and comparison of the electronic structures of **1** and **2** and the covalent bonding of Ti or Th with the Al center are discussed.

## MATERIALS AND METHODS

**Sample Preparation.** Complexes **1a**, **1b**, and **2** were synthesized and characterized as in previous studies.<sup>24,25</sup> To make EPR samples, 2 mM toluene solutions of these compounds were transferred into EPR sample tubes in a glovebox with  $\text{O}_2/\text{H}_2\text{O} < 0.5$  ppm. The tubes were flame-sealed and stored in liquid nitrogen prior to use.

**EPR Spectroscopy.** EPR spectroscopy was performed in the CalEPR center in the Department of Chemistry, University of California at Davis. Continuous-wave (CW) EPR spectra were recorded on a Bruker Biospin EleXsys E500 spectrometer with a superhigh Q resonator (ER4122SHQE) in perpendicular mode.

Cryogenic temperature was achieved by using an ESR900 liquid-helium cryostat with a temperature controller (Oxford Instrument ITC503) and a gas flow controller. All CW EPR spectra were recorded under slow-passage, nonsaturating conditions. Spectrometer settings were as follows: conversion time = 40 ms, modulation amplitude = 0.3 mT, modulation frequency = 100 kHz, and parameters in the corresponding figure legends. Pulse Q-band ENDOR experiments were performed on the Bruker Biospin EleXsys 580 spectrometer equipped with a R. A. Isaacson cylindrical TE<sub>011</sub> resonator.<sup>28</sup> The following pulse sequences were employed: free-induction-decay field-swept EPR ( $\pi/2$ –FID), electron spin–echo-detected field-swept EPR ( $\pi/2$ – $\tau$ – $\pi$ – $\tau$ –echo), and Davies ENDOR ( $\pi$ –RF– $\pi/2$ – $\tau$ – $\pi$ – $\tau$ –echo). Simulations of CW and pulse EPR spectra were performed in *Matlab 2014a* with the *EasySpin 5.1.10* toolbox.<sup>29</sup> Euler angles relate the principal coordination system of A tensors to g tensors and follow the yz convention.

For nuclei with nuclear spin  $I = 1/2$  ( $^1\text{H}$  in this study), the ENDOR transitions for the  $m_s = \pm 1/2$  electron manifolds are observed, to a first-order approximation, at the frequencies  $\nu_{\pm} = \nu_N \pm A/2$ , where  $\nu_N$  is the nuclear Larmor frequency and  $A$  is the orientation-dependent hyperfine coupling.<sup>30</sup> In the weak coupling limit [ $\nu_N > A/2$ , exemplified by all of the  $^1\text{H}$  HFIs presented in this study], the ENDOR peaks are centered at  $\nu_N$  and separated by  $A$ . In the strong coupling limit ( $\nu_N < A/2$ , as seen, for example, for  $^{27}\text{Al}$  in **2** in this study), the ENDOR peaks are centered at  $A/2$  and separated by  $2\nu_N$ . For nuclei with  $I > 1/2$  (for  $^{27}\text{Al}$ ,  $I = 5/2$  in this study), the two ENDOR branches are further split by the orientation-dependent nuclear quadrupole interaction (NQI,  $\mathbf{P}$ ), defined as  $\mathbf{P} = [P_1, P_2, P_3] = e^2Qq/4I(2I - 1)\hbar \times [-1 + \eta, -1 - \eta, 2]$  with the asymmetry parameter  $\eta = (P_1 - P_2)/P_3$ , ranging from 0 to 1, corresponding to an axially symmetric and rhombic electric field gradient at the nucleus, respectively. The frequencies for the  $m_1 \leftrightarrow (m_1 - 1)$  ENDOR transition are observed at  $\nu_{\pm, m_1} = \nu_N \pm A/2 \pm (3P/2)(2m_1 - 1)$ , which gives a total of 10 ENDOR peaks for  $^{27}\text{Al}$  at each field position. At the edges of the absorption envelope where the EPR spectra are “single-crystal-like”, these peaks are usually well-resolved. At other field positions, however, ENDOR peaks are usually broadened and overlapped, and spectral simulations are necessary to extract the parameters.

The signs of the  $^1\text{H}$  hyperfine tensors were determined by variable-mixing-time (VMT) Davies ENDOR experiments.<sup>30</sup> In VMT Davies ENDOR, different mixing times after the radio-frequency (RF) pulse are used. With longer mixing time, relaxation of the  $\alpha$ -electron-spin manifold ( $m_s = +1/2$ ) decreases the ENDOR signal intensity (relative to the other ENDOR peak) corresponding to this manifold. The larger observed ENDOR frequency ( $\nu_+$ ) corresponds to the  $\alpha$ -electron-spin manifold (and, hence, has decreased relative intensity at elongated mixing time) if  $A < 0$  and vice versa.

**Computational Details.** The EPR parameters for compounds **1a** and **2** are calculated in ORCA 4.0.1.<sup>31</sup> Previously optimized geometries of **1a** and **2** were adopted for calculations.<sup>24,25</sup> The electronic structure and spectroscopic parameters were calculated at the DFT level using the unrestricted Kohn–Sham formalism and employing the hybrid meta-generalized-gradient-approximation TPSSH wave functional<sup>32</sup> along with the chain-of-sphere (RJCOSX) approximation.<sup>33</sup> Triple- $\zeta$  valence polarization def2-TZVP basis sets and the decontracted auxiliary basis sets def2/J coulomb fitting<sup>34</sup> were used. The basis set of EPR-II was used for all H atoms, and the basis set of cc-PCVTZ (triple- $\zeta$  with core correlation) was used for Ti and Al atoms. For compound **2**, the all-electron scalar relativistic basis set SARC-ZORA-TZVP was used for the Th atom with the SARC/J coulomb-fitting auxiliary basis sets.<sup>35–38</sup> The zero-order regular approximation (ZORA) was used to account for the scalar relativistic effects. Increased integration grids (Grid4 and GridX4 in ORCA convention) and tight self-consistent-field convergence were used throughout the calculation of all EPR parameters. The conductor-like polarizable continuum model (CPCM) was used to model the dielectric effects from the solvent toluene ( $\epsilon = 2.38$ ) used for EPR

samples. Typical input files including the coordinates are shown in the Supporting Information (SI).

## RESULTS

**1.  $\text{Ti}^{3+}$ –Al Complexes (**1a** and **1b**). 1.1. EPR Characterization.** The X-band (9.4 GHz) liquid-phase CW EPR spectrum of **1a** recorded at 200 K in a 2 mM toluene solution is dominated by a complex multiline pattern (Figure 1A),

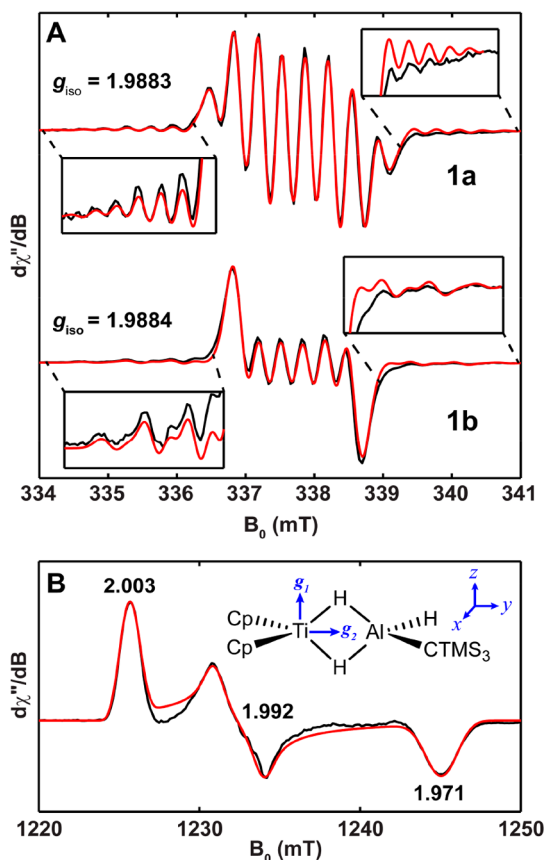


**Figure 1.** EPR spectra of **1a** and **1b**. (A) X-band CW EPR spectra of **1a** (top) and **1b** (bottom) recorded at 200 K (black traces) and simulations (red traces). The wing regions of the spectra showing Ti HFI are shown in the zoomed-in insets. (B) Pseudomodulated Q-band FID-detected EPR spectra of **1a** recorded at 30 K (black trace) and simulation (red trace). The directions of the principal  $g$  values are noted in part B. The  $xyz$  frame is chosen as  $g_1 = g_z$ . Parameters: (A), microwave power = 0.02 mW; modulation amplitude = 0.1 mT; (B)  $\pi/2 = 1 \mu\text{s}$ ; modulation amplitude = 0.5 mT.

which arises from the hyperfine couplings to aluminum ( $^{27}\text{Al}$ : 100%,  $I = 5/2$ ) and the bridging hydrides ( $^1\text{H}$ ,  $I = 1/2$ ). The spectrum also contains two “wings” flanking the central region (zoom-in insets in Figure 1A), which can be attributed to the hyperfine couplings from the two most-common magnetic isotopes of Ti ( $^{47}\text{Ti}$ , 7.44%,  $I = 5/2$ ;  $^{49}\text{Ti}$ , 5.41%,  $I = 7/2$ ). The solution EPR spectrum is well-simulated by using an isotropic  $g$  value of  $g_{\text{iso}} = 1.9984$  and four isotropic HFI values of  $|a_{\text{iso}}|$  [ $^{47}\text{Ti}$ ,  $^{27}\text{Al}$ ,  $^1\text{H}$ ,  $^1\text{H}$ ] = [17.4, 9.4, 9.8, 9.8] MHz.<sup>39</sup> These spectral simulation parameters are corroborated by the CW EPR spectrum of compound **1b** in which the hydrides in the alanate ligand are replaced by deuterides ( $^2\text{H}$ :  $I = 1$ ). The central pattern and flanking wings of the solution EPR spectrum of **1b** indicate hyperfine couplings from  $^{27}\text{Al}$ ,  $^2\text{H}$ ,

and Ti. Simulation of this spectrum reveals the same isotropic  $g$  value of  $g_{\text{iso}} = 1.9983$  and also four isotropic HFI values:  $|a_{\text{iso}}|$  [ $^{47}\text{Ti}$ ,  $^{27}\text{Al}$ ,  $^2\text{H}$ ,  $^2\text{H}$ ] = [17.4, 9.0, 1.5, 1.5] MHz. These parameters are essentially identical with those determined in **1a**, and especially the  $a_{\text{iso}}$  value of  $^2\text{H}$  matches well with that of  $^1\text{H}$  in **1a** scaled by the ratio of their nuclear  $g$  values ( $g_n$ ;  $^2\text{H}$ : $^1\text{H}$  = 1:6.51). The solution CW EPR spectra of **1a** and **1b** represent one of the few examples where the  $a_{\text{iso}}$   $^{27}\text{Al}$  values are clearly resolved in the CW EPR spectra<sup>40–42</sup> and a rare case showing the Ti hyperfine coupling.<sup>43</sup>

At cryogenic temperature (30 K), the  $g$  anisotropy of **1a** and **1b** in the solid state is revealed. In the Q-band FID-detected EPR spectra (Figure 1B), both **1a** and **1b** have a rhombic  $g$  tensor = [2.003, 1.992, 1.971], which exactly satisfy the relationship  $g_{\text{iso}}^2 = 1/3(g_1^2 + g_2^2 + g_3^2)$ , indicating a conserved electronic structure at lower temperatures. These values are consistent with the  $3d^1$  configuration of the  $\text{Ti}^{3+}$  ion with a  $d_{z^2}$  ground state because the largest principal  $g$  value ( $g_1$ ) is almost identical with that of the free electron ( $g_e = 2.0023$ ). The  $g$  tensor is also similar to that found in the single-crystal EPR study of the vanadium(IV) metallocenes ( $\text{Cp}_2\text{VCl}_2$ ) doped into the corresponding  $\text{Ti}^{4+}$  diamagnetic host.<sup>44,45</sup> On the basis of the single-crystal EPR study of  $\text{Cp}_2\text{VCl}_2$  and the EPR characterization of another titanium(3+) metallocene,  $\text{Cp}_2\text{TiOAc}$ ,<sup>46</sup> the directions of the principal  $g$  values of **1a** are assigned as follows: the intermediate  $g$  value,  $g_2 = 1.992$ , lies in the Ti–H–H plane and bisects the H–Ti–H angle; the largest  $g$  value,  $g_1 = 2.003$ , lies also in this plane, perpendicular to the plane formed by two Cp centroids and the Ti center (Figure 1B). This assignment is consistent with the molecular orbital (MO) description of **1a** from both the well-understood frontier orbitals of bent metallocenes<sup>46,47</sup> and our DFT calculations: the singly occupied molecular orbital (SOMO) of **1a** is a nonbonding  $a_1$  orbital dominated by Ti  $3d_{z^2}$ , and the  $g_1$  that we assigned is coaxial to the longitudinal lobe of the  $3d_{z^2}$  orbital.<sup>25</sup>

**1.2.  $^1\text{H}$  ENDOR.** The  $^1\text{H}$  HFI observed in the solution CW EPR of **1a** was further analyzed by field-dependent Q-band Davies ENDOR spectra collected across the absorption envelope of frozen samples of **1a** and **1b** in order to extract the hyperfine tensors. The ENDOR features in the outer region of the spectra are present in the spectra of **1a** (Figure 2A, black trace), but not **1b** (Figure 2A, blue trace), and therefore must be attributed to the bridging hydrides. This is one of a few examples of  $^1\text{H}$  HFI analyzed by ENDOR in metal hydrides.<sup>48–53</sup> The terminal hydride, the protons from the Cp rings, and the  $\text{CTMS}_3$  moiety contribute to the central regions of the ENDOR spectra.

**Bridging Hydride  $^1\text{H}$  HFI.** Although there are two bridging hydrides in **1a**, their HFI tensors are likely to be similar because of the presence of a pseudo mirror plane. Indeed, the outer region of the ENDOR spectra of **1a** can be well-simulated with one  $^1\text{H}$  HFI tensor (Figure 2A, red trace) of  $A^1\text{H} = [6.8, -15.2, -20.7]$  MHz with Euler angles of  $[63, 3, 0]^\circ$  relative to the  $g$  frame (Table 1). Decomposition of  $A$  gives an  $a_{\text{iso}}$  of  $-9.7$  MHz that is consistent with the value determined from CW EPR and an anisotropic component of  $T = [16.5, -5.5, -11.0]$  MHz. The relative signs of the principal  $A$  values are determined by spectral simulation; the absolute sign of  $A$  is determined by VMT Davies ENDOR spectra collected at  $g_3$ , where  $A_{\text{max}}$  is observed (Figure 2B). As the mixing time is increased from 1 to 200  $\mu\text{s}$ , the relative intensity of the ENDOR peak at higher RF decreases (Figure 2B), which is a



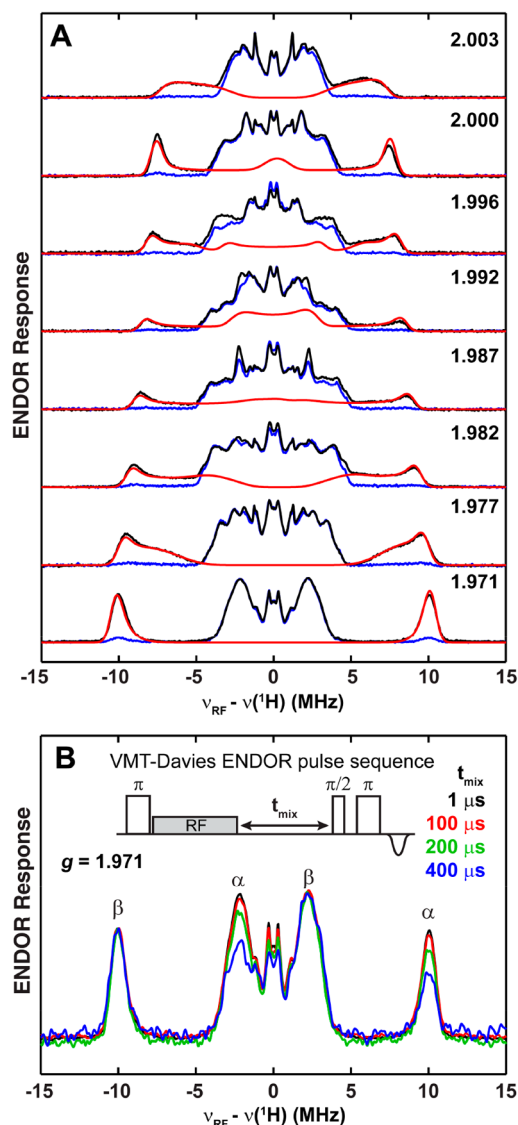


**Figure 2.**  $^1\text{H}$  Davies ENDOR spectra of **1a** and **1b**. (A) Q-band field-dependent Davies ENDOR spectra of **1a** (black trace) and **1b** (blue trace) and simulation for the bridging hydrides (red trace). (B) VMT Davies ENDOR spectra of **1a** collected at  $g = 1.971$  using different  $t_{\text{mix}}$  values. Spectra are normalized with respect to the low-frequency ENDOR manifold of the bridging hydride. Parameters: temperature = 25 K, inversion pulse = 80 ns,  $\pi/2$  pulse = 12 ns,  $\tau = 300$  ns, RF pulse = 15  $\mu\text{s}$ . Simulation:  $g = [2.003, 1.992, 1.971]$ ;  $A^1\text{H} = [6.8, -15.2, -20.7]$  MHz; Euler angles =  $[63, 3, 0]^\circ$ .

characteristic of the corresponding nuclear spin-flip transition being between levels within the  $\alpha$ -electron-spin manifold, and therefore the sign of  $A_3$  has to be negative. This result is reasonable with a positive  $T_{\text{max}}$  (16.5 MHz) for  $^1\text{H}$  ( $g_n > 0$ ) because  $T$  is dominated by the through-space electron–nuclear dipolar interaction. According to the  $g$ -frame directionality assigned above, the Euler angle used in the optimized simulation indicates that **A** is rotated primarily within the  $g_1$ – $g_2$  plane (Ti–H–H plane) along the  $g_3$  axis for  $63^\circ$  ( $\alpha = 63^\circ$ ) but tilted slightly out of the plane ( $\beta = 3^\circ$ ). Given the H–Ti–H angle of  $72^\circ$  as observed in the X-ray structure of **1a**,<sup>25</sup> the resulting orientation of the  $^1\text{H}$   $A$  tensor essentially gives an  $A_1$  pointing from the Ti center to one of the bridging H atom (Figure S1), which is consistent with  $T_1$  (16.5 MHz) being the

**Table 1.** Summary of the EPR Parameters for **1a** and **2**

	<b>1a</b>	<b>2</b>
$g$ values	[2.003, 1.992, 1.971]	[1.967, 1.899, 1.788]
$\mu^1\text{H}$		
$a_{\text{iso}}^a$	−9.7	−10.7
$A^{a,b}$	$[6.8, -15.2, -20.7] \pm 0.1$	$[-6.0, -11.1, -15.0] \pm 0.1$
$[\alpha, \beta, \gamma]^{o,b}$	$[63, 3, 0] \pm 2$	$[103, 30, 0] \pm 2$
$^{27}\text{Al}$		
$a_{\text{iso}}^a$	9.4	34
$A^{a,b}$	$[6.0, 14.6, 7.6] \pm 0.1$	$[23, 46, 33] \pm 1$
$[\alpha, \beta, \gamma]^{o,b}$	$[90, 10, -90] \pm 5$	$[35, 35, -35] \pm 5$
$e^2Qq/h^{a,b}$	$20.0 \pm 1$	$\sim 20$
$[\alpha, \beta, \gamma]^{o,b}$	$[90, 25, -90] \pm 5$	0
$\eta$	0.34	$\sim 0$

<sup>a</sup>HFI and NQI parameters are in megahertz. <sup>b</sup>Errors were estimated from spectral simulation.

largest principal  $T$  value. It also suggests that the two hydrides are locked in a static symmetric  $\text{MH}_2$  system at the temperature of the ENDOR experiments (25 K), in contrast to the free rotating  $\text{H}_2$  found in a cobalt– $\text{H}_2$  complex.<sup>54</sup> Our DFT calculation gives  $A^1\text{H} = [12.7, -11.3, -17.2]$  and  $[11.9, -12.3, -18.3]$  MHz (Table S1), which are reasonably consistent with the ENDOR-derived results. These two predicted values are also very similar, supporting the fact that we only observe one set of  $^1\text{H}$  values.

The negative  $a_{\text{iso}}$ , −9.7 MHz, corresponds to a small s-orbital spin density of  $-6.8 \times 10^{-3}$  on each bridging hydride atom ( $a_0^1\text{H} = 1420$  MHz<sup>55</sup>). The relatively small  $|a_{\text{iso}}|$  of this hydride species could be explained by the MOs of bent metallocenes as previously described, which suggested that the hydrides in such  $\text{Cp}_2\text{MH}_2$  molecules with a  $d^1$  electron configuration lie close to the nodal cone of the singly occupied  $d_z^2$  orbital, leading to a small Fermi contact.<sup>47</sup> The negative sign of  $a_{\text{iso}}$  also indicates that the spin on the bridging hydride arises mainly from a spin-polarization mechanism, which leads to excess  $\beta$  spin on the hydrides.

The anisotropic component of  $^1\text{H}$  HFI arises solely from the through-space electron–nuclear dipolar interactions due to the absence of any local contribution from p-, d-, and f-type orbitals. For a mononuclear  $\text{Ti}^{3+}$  center with very small  $g$  anisotropy, as in the case of **1a**, if the distance between  $\text{Ti}^{3+}$  and the magnetic nuclei is large ( $r > 2.5$  Å), the point-dipole approximation would lead to an axial  $T = [2T, -T, -T]$ , where  $T = \rho_{\text{Ti}} g_{\text{e}} g_{\text{n}} \beta_{\text{e}} \beta_{\text{n}} / r^3$  ( $\rho_{\text{Ti}}$  is the spin density on Ti).<sup>56</sup> This approximation does not hold in the case of **1a** because the distances between the bridging hydrides and the  $\text{Ti}^{3+}$  center are relatively short (averaged  $r_{\text{Ti-H}} = 1.892$  Å). As a result, the experimental  $T$ ,  $[16.5, -5.5, -11.0]$  MHz, is fairly rhombic. This rhombicity in  $T$  can be modeled using the empirical approximation previously applied to the  $2p_z$  orbital;<sup>57</sup> that is, we assume that the spin-density distribution in the Ti  $3d_z^2$  orbital can be treated as three discrete spin centers on the  $z$  axis (Figure 3): A and C at  $(0, 0, \pm r_A)$  represent the two longitudinal lobes of  $3d_z^2$  with  $\rho_A = \rho_C = 0.25\rho_{\text{Ti}}$  and B at  $(0, 0, 0)$  represents the donut shape near the nucleus with  $\rho_B = 0.5\rho_{\text{Ti}}$ . Three point-dipole interactions generated from these spin centers,  $T_A$ ,  $T_B$ , and  $T_C$ , are summed to give the total  $T_{\text{cal}}$  (see the SI):<sup>58</sup>  $T_{\text{cal}} = \rho_A T_A + \rho_B T_B + \rho_C T_C$ . If we use  $\rho_{\text{Ti}} \sim 0.95$  (obtained from the DFT calculation) and by varying  $r_A$ , the best match to the experimental  $T$  is obtained when  $r_A = 1.4$  Å, which yields  $T_{\text{cal}} = [16.6, -5.3, -11.3]$  MHz. In comparison, the  $r_A$  value used for the C  $2p_z$  orbital in the previous study was

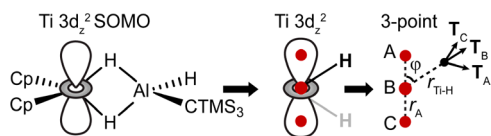


**Figure 3.** Illustration of the three-point-dipole model to describe the spin-density distribution on the Ti  $3d_z^2$  orbital in **1a**. In this case,  $r_{\text{Ti-H}} = 1.89$  Å,  $r_A = 1.4$  Å, and  $\varphi = 54^\circ$ . The unique axes for the dipolar contribution from each point (A–C) are noted as  $T_A$ ,  $T_B$ , and  $T_C$ , respectively.

0.68 Å.<sup>57</sup> A calculation study on the spin polarizations of different atomic orbitals suggested that the radial distribution of a singly occupied 3d orbital is about twice as large as that of the 2p orbitals,<sup>59</sup> which provides some basis for the magnitude of this  $r_A$  value. To further test if our model is reasonable in other systems with half-filled  $3d_z^2$ , we applied this method to analyze the  $^1\text{H}$  HFI of the bridging hydride in the Ni–C state of the [NiFe] hydrogenase.<sup>53</sup> The three-point model agrees well with the experimental results ( $T_{\text{exp}} = [21.9, -7.3, -14.5]$  MHz,  $T_{\text{cal}} = [16.9, -6.0, -10.9]$  MHz; see the SI for details). In both cases, this empirical treatment rationalizes the origin of the  $^1\text{H}$  hyperfine anisotropy for a hydride bound to a  $(3d_z^2)^1$  configuration metal center.

**Cp Ring  $^1\text{H}$  HFI.** The major features in the  $^1\text{H}$  ENDOR spectra of **1b** arise from the  $^1\text{H}$  on the Cp rings, which are closer to Ti (2.94 Å on average) than the protons in the CTMS<sub>3</sub> moiety ( $\sim 5$ –8 Å). Because of the number of different  $^1\text{H}$  on the Cp rings, we analyze the HFI of these  $^1\text{H}$  by combining the ENDOR experiments with the DFT calculations. The DFT-calculated spin densities of Cp C atoms and HFI of Cp  $^1\text{H}$  are summarized in Table S1 and Figure S2.

A previous study suggested that Cp  $^1\text{H}$  HFI may stem from both the through-space dipolar interactions with the spin center and the spin polarization of the C–H bonding electrons by the C  $2p_\pi$  spin density.<sup>23</sup> The former gives  $T \sim 2.8$  MHz with a point-dipole approximation or  $\sim 2.2$ –3.0 MHz using the three-point-dipole model (vide supra). The DFT-calculated Cp  $^1\text{H}$  HFIs are all predicted to have anisotropy consistent with our three-point-dipole model, especially for  $^1\text{H}$  on C1 and C3 of the Cp ligand (see the SI) where C spin densities are close to zero (Table S1 and Figure S2). ENDOR spectra of **1b** collected in resonance with  $g_2$  exhibit  $^1\text{H}$  A values as large as  $\sim 9$  MHz (Figure 2A), indicating that other hyperfine mechanisms, in addition to the dipolar interactions, contribute. DFT predictions of the HFI for protons bound to C2 and C5 reproduce these A values. The DFT results also predict that these A values and  $a_{\text{H}}$  values of Cp  $^1\text{H}$  are positive, as observed by VMT Davies ENDOR spectra recorded at different field positions (Figure S3). The positive  $a_{\text{H}}$  values cannot be traced to a spin-polarization process of the McConnell type alone because the DFT-predicted spin densities of  $\sim 0.02$  on C2/C5 (Figure S2) would only give rise to much smaller  $a_{\text{H}}$  values of negative sign. Rather, direct spin delocalization of  $\text{Ti}^{3+}(d_z^2) \rightarrow \text{Cp}(e_{2g})$ , i.e., the Cp character in the  $1a_1$  MO, could mainly be responsible for the positive hyperfine values on Cp protons. This spin-delocalization mechanism may be analogous to the hyperconjugation mechanism that accounts for the positive  $^1\text{H}$  HFI of the  $\beta$ -protons in organic radicals.<sup>60</sup>

According to these analyses and the results from calculations, we roughly simulate the ENDOR spectra of **1b** with three sets of HFI tensors corresponding to  $^1\text{H}$  on C1, C2/

C5, and C3/C4 (Figure S4), which reproduces most features in the ENDOR spectra.

**1.3.  $^{27}\text{Al}$  ENDOR.** The field-dependent Davies ENDOR spectra of **1a** in the low-frequency region (2–30 MHz) exhibit wide features that are attributed to the HFI and NQI of  $^{27}\text{Al}$  ( $I = 5/2$ ; Figure 4). Notably, at the “single-crystal-like”  $g_1$  edge,

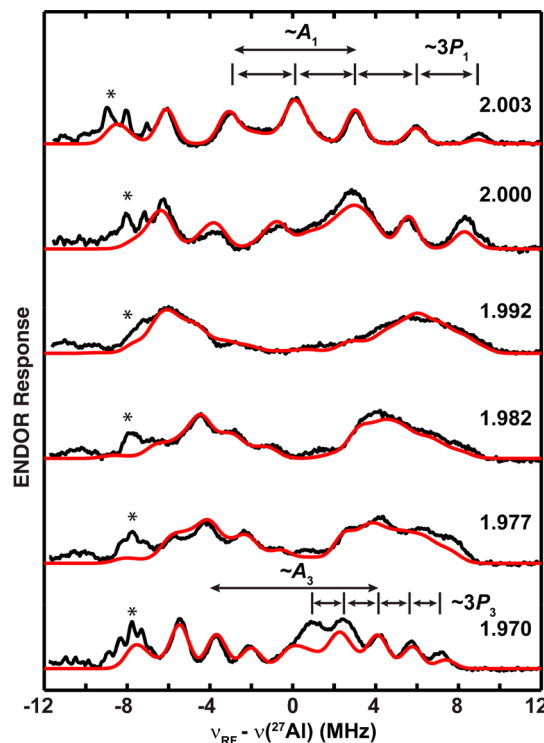


**Figure 4.** Q-band  $^{27}\text{Al}$  Davies ENDOR of **1a** (black traces) and simulations (red traces).  $A_1/P_1$  and  $A_3/P_3$ , which can be approximately read off from the spectra, are marked at  $g_1$  and  $g_3$ , respectively. Al ENDOR features marked by asterisks arise from NMR flip–spin transitions induced by the third harmonic of normal RF excitation frequencies. Parameters: inversion pulse = 80 ns,  $\pi/2$  pulse = 12 ns,  $\tau = 300$  ns, and RF pulse = 30  $\mu\text{s}$ . Simulation:  $g = [2.003, 1.992, 1.971]$ ,  $A^{27}\text{Al} = [6.0, 14.6, 7.6]$  MHz, Euler angle =  $[90, 10, -90]^\circ$ ,  $P = [1.00, -0.33, -0.67]$  MHz, and Euler angle =  $[90, 25, -90]^\circ$ .

the ENDOR peaks are uniformly spaced by the orientation-dependent NQI splitting,  $3P_1 = 3$  MHz, representing a rare example of a well-resolved  $^{27}\text{Al}$  ENDOR spectrum with a well-resolved NQI pattern.<sup>61–63</sup> The large NQI splitting cause an overlap between the two ENDOR branches. Similar patterns are seen at the  $g_3$  edge with  $3P_3 \sim 2$  MHz. With these parameters that can be read off from the ENDOR spectra and the  $^{27}\text{Al}$   $a_{\text{iso}}$  from CW EPR, the ENDOR spectra are well-simulated using  $A^{27}\text{Al} = [6.0, 14.6, 7.6]$  MHz with Euler angles of  $[90, 10, -90]^\circ$ , and  $P^{27}\text{Al} = [1.00, -0.33, -0.67]$  MHz with Euler angles of  $[90, 25, -90]^\circ$ . The orientation of **A** is consistent with that of **A**<sub>2</sub> along the Ti–Al vector, whereas the unique axis of **P** is close to that of the Al–CTMS<sub>3</sub> vector. The ENDOR spectrum of **1b** is essentially the same as that of **1a**, except that in **1b** extra ENDOR signals arising from the bridging  $^2\text{H}$  are overlaid with the  $^{27}\text{Al}$  signals and are consistent with the bridging  $^1\text{H}$  HFI in **1a** scaled by the ratio of their nuclear  $g_n$  values (Figure S5).

**$^{27}\text{Al}$  HFI.** A  $^{27}\text{Al}$  of  $[6.0, 14.6, 7.6]$  MHz can be decomposed into the isotropic part,  $a_{\text{iso}} = 9.4$  MHz, and the dipolar part,

$T_{\text{dip}} = [-3.4, 5.2, -1.8]$  MHz. The isotropic hyperfine coupling corresponds to a small Al 3s orbital spin density of  $2.4 \times 10^{-3}$  using  $a_0 = 3911$  MHz for one unpaired electron on the Al 3s orbital. The dipolar part has two major contributions: (1) the nonlocal through-space electron–nuclear dipolar interaction between the  $\text{Ti}^{3+}$  center and Al, which are separated by  $r_{\text{Ti-Al}} = 2.78$  Å,  $T_{\text{nl}}$ ; (2) the local contribution from the 3p orbital spin density on Al,  $T_{\text{loc}}$ . These two components are not necessarily coaxial with one another. The nonlocal component (here  $T_{\text{nl}} = [-T, 2T, -T]$  because  $A_2$  is pointing along the Ti–Al vector) can be estimated using the relationship  $T = \rho_{\text{Ti}} g_{\text{Ti}} \beta_{\text{N}} \beta_{\text{N}} / r^3 = 0.9$  MHz. Subtracting  $T_{\text{nl}}$  from  $T_{\text{dip}}$  yields  $T_{\text{loc}} = [-2.5, 3.4, -0.9]$  MHz, which gives a total spin density in the three Al 3p orbitals of  $\sim 0.03$ , following previous procedures<sup>64</sup> as detailed in the SI. Because the 3p spin density is much larger than the 3s contribution, the total spin density on Al is also  $\sim 0.03$ .

<sup>27</sup>Al NQI. The <sup>27</sup>Al ENDOR spectra reveal an <sup>27</sup>Al NQI tensor of  $\mathbf{P} = [1.00, -0.33, -0.67]$  MHz, which can be written in another form as  $\mathbf{P} = (e^2 Q q / h) / [4I(2I - 1)][2, -1 + \eta, -1 - \eta]$ , corresponding to  $e^2 Q q / h = 20.0$  MHz and  $\eta = 0.34$ . These NQI parameters match well with the DFT calculations (Table S1) and are analyzed in the SI.

## 2. Th–Al Heterometallic Complex (Compound 2).

**2.1. EPR Characterization.** The EPR analysis of **1a** framed our thinking for the more complicated Th system. The EPR spectra of **2** were reported previously<sup>25</sup> and are reproduced here in Figure S6. The 200 K solution spectrum gives a broad peak with  $g_{\text{iso}} = 1.886$ , and the 50 K frozen solution spectrum reveals the rhombic  $\mathbf{g} = [1.967, 1.899, 1.788]$ , which also satisfies  $g_{\text{iso}}^2 = 1/3(g_1^2 + g_2^2 + g_3^2)$ . These values are consistent with a  $6d_{z^2}$  ground state, as found in other  $\text{Th}^{3+}$  complexes,<sup>22</sup> and agree reasonably with the DFT-calculated  $\mathbf{g}$  values ( $[1.985, 1.900, 1.823]$ ; Table S2). The deviation of  $g_1$  from  $g_e$  is not unprecedented in  $\text{Th}^{3+}$  complexes (Table S3) and may be caused by high-order spin–orbital coupling or mixing of other d orbitals into the SOMO. In line with the Ti complex and the  $(\text{Cp}^{\text{tt}})_3\text{Th}$  complex reported previously,<sup>23</sup> the directions for the  $\mathbf{g}$  frame could be assigned as indicated in Figure S6; that is,  $g_1$  ( $g_z$ ) is perpendicular to the plane constituted by Th and the two centroids of the  $\text{Cp}^{\text{tt}}$  ring, and  $g_2$  is approximately pointing along the Th–Al vector. For comparison, the spin–lattice relaxation time constant ( $T_1$ ) of **2** was determined to be 972  $\mu\text{s}$  at 10 K and 194  $\mu\text{s}$  at 15 K, similar to the values reported for the  $(\text{Cp}^{\text{tt}})_3\text{Th}$  complex (1100  $\mu\text{s}$  at 11 K).<sup>23</sup>

**2.2. <sup>1</sup>H ENDOR.** The <sup>1</sup>H region of the ENDOR spectra of **2** contains two major sets of signals that are just separated, as shown in Figure 5A. In light of the ENDOR spectra of **1a**, the ENDOR signals with larger HFI,  $\sim 10$ – $15$  MHz, mostly likely arise from bridging hydrides. This assignment is also supported by comparing the ENDOR spectra of **2** to the reported HSCORE spectra of  $(\text{Cp}^{\text{tt}})_3\text{Th}$  showing <sup>1</sup>H HFI from the same ligands, with <sup>1</sup>H HFI < 5 MHz.<sup>23</sup>

**Bridging <sup>1</sup>H HFI.** The three hydrides in **2** adopt two different conformations (Scheme 1): one lies on the plane constituted by the Th atom and two  $\text{Cp}^{\text{tt}}$  centroids, while the other two are located at each side of this plane. Despite such asymmetry, the sharp peaks on the ENDOR spectra collected at both the  $g_1$  and  $g_3$  edges indicate that the ENDOR signals can be attributed to a single set of <sup>1</sup>H HFIs, simulated to be  $\mathbf{A}^{\text{H}} = [-6.0, -11.1, -15.0]$  MHz with Euler angles of  $[103, 30, 0]^\circ$  (Figure 5A). Decomposition of this  $\mathbf{A}$  tensor gives  $a_{\text{iso}} = -10.7$  MHz and  $\mathbf{T} = [4.7, -0.4, -4.3]$  MHz. Similar to the Ti

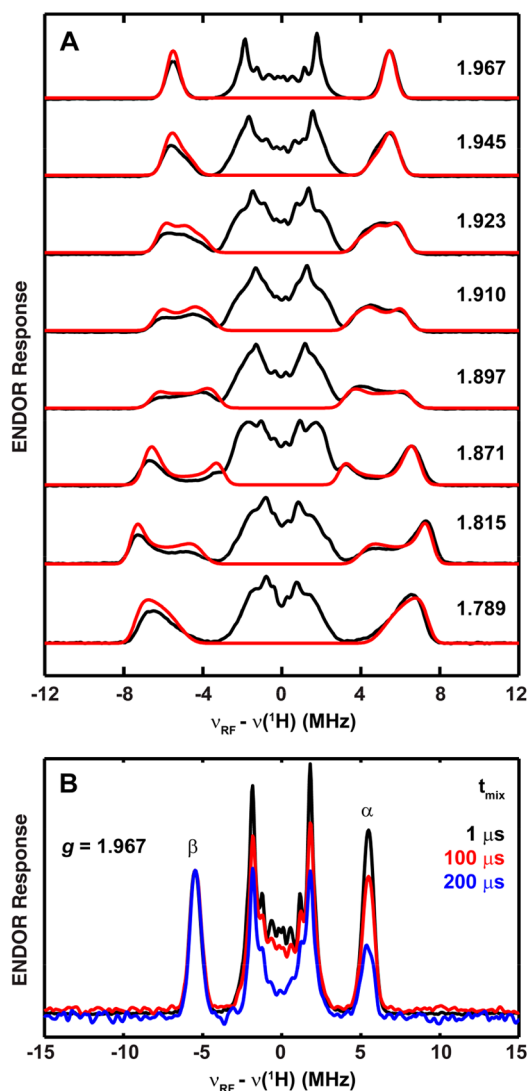


**Figure 5.** <sup>1</sup>H Davies ENDOR spectra of **2**. (A) Q-band field-dependent Davies ENDOR spectra of **2** (black trace) and simulation for the bridging hydrides (red trace). (B) VMT Davies ENDOR spectra of **2** collected at  $g = 1.967$  using different  $t_{\text{mix}}$ . Spectra are normalized with respect to the low-frequency ENDOR manifold of the bridging hydrides. Parameters: temperature = 15 K, inversion pulse = 80 ns,  $\pi/2$  pulse = 12 ns,  $\tau = 300$  ns, and RF pulse = 15  $\mu\text{s}$ . Simulation:  $\mathbf{g} = [1.967, 1.899, 1.788]$ ,  $\mathbf{A}^{\text{H}} = [-6.0, -11.1, -15.0]$  MHz, and Euler angle =  $[103, 30, 0]^\circ$ .

complex, the signs of  $\mathbf{A}$  are determined by VMT Davies ENDOR spectroscopy collected at  $g_1$  (Figure 5B).

The negative  $a_{\text{iso}}$ ,  $-10.7$  MHz, corresponds to an s orbital spin density of  $-7.5 \times 10^{-3}$  on each bridging hydride. This gives a total spin density of merely  $-2.3 \times 10^{-2}$  on the three hydrides. The dipolar part of the hyperfine tensor is close to a fully rhombic  $[T, 0, -T]$  form, despite an averaged Th–H distance of 2.45 Å, which is usually long enough for point-dipole approximation. This rhombicity is probably caused by the highly diffuse nature of the spin-carrying Th  $6d_{z^2}$  orbital, undercutting the accuracy of the point-dipole approximation. The  $\sim 0.15$  spin density on the Al (vide infra) may also have a small contribution to the rhombicity if being considered as a secondary spin center.<sup>48</sup> If we just consider the spin density on Th, using the three-point-dipole model mentioned above and



$\rho_{\text{Th}} \sim 0.8$  from DFT calculations, this T tensor can be reproduced with an empirical  $r_A$  of  $\sim 3$  Å and a resulting  $T_{\text{cal}} = [4.8, -0.5, -4.3]$  MHz. This empirical  $r_A$  value implies that the radial distribution of the Th 6d orbital could be more than twice that of the Ti 3d orbital.

**Cp  $^1\text{H}$  HFI.** The central region of the ENDOR spectra of **2** represents HFI from  $^1\text{H}$  on the Cp<sup>tt</sup> ligands and tBu groups. The averaged HFI values of  $\sim 4$  MHz are essentially consistent with the reported  $^1\text{H}$  HYSCORE for (Cp<sup>tt</sup>)<sub>3</sub>Th.<sup>23</sup> In this case, however, the VMT Davies ENDOR spectra shown in Figure S7 indicate that the  $a_{\text{H}}$  values of the Cp<sup>tt</sup> protons are negative, indicating a hyperfine mechanism dominated by spin polarization of the C–H bonding electrons by the Cp<sup>tt</sup> C 2p <sub>$\pi$</sub>  spin density, as pointed out by the previous study on the (Cp<sup>tt</sup>)<sub>3</sub>Th complex.<sup>23</sup> The differences between **1a** and **2** thus reflect a larger spin density on the aromatic C atoms in the Th complex (see the SI for DFT results), caused again by the more diffuse 6d orbitals, leading to more Cp character in the SOMO.

**2.3.  $^{27}\text{Al}$  ENDOR.** The field-dependent Q-band  $^{27}\text{Al}$  Davies ENDOR spectra of **2** are shown in Figure 6. Here, the much larger  $^{27}\text{Al}$  HFI quantifies the system as being in the strong coupling case,  $A > 2\nu_{\text{Al}}$ , and only the higher-frequency ENDOR transitions at  $\sim 25$ –40 MHz are recorded. The low-frequency ENDOR transitions, simulated to be centered at  $\sim 4$ –5 MHz, have weak signal intensity and are complicated by

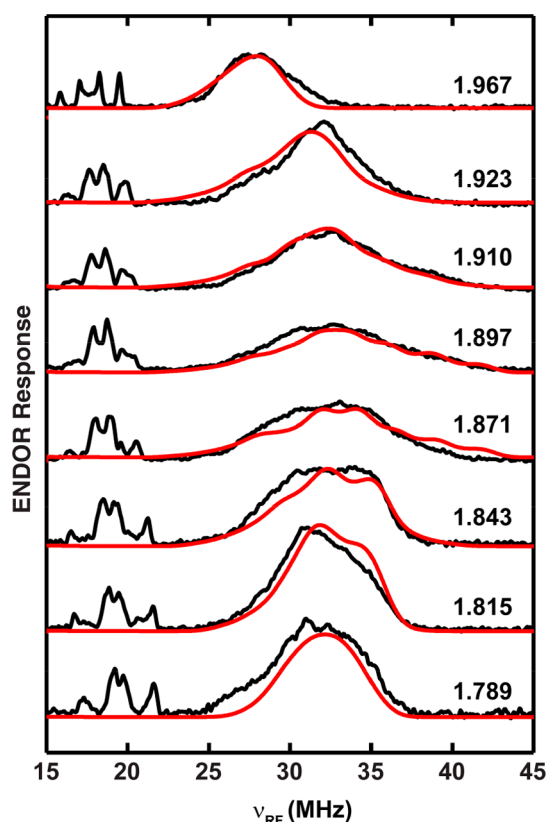


**Figure 6.** Q-band  $^{27}\text{Al}$  Davies ENDOR spectra of **2** (black trace) and simulation of the  $^{27}\text{Al}$  HFI (red trace). Features at 15–22 MHz are the contributions from the third harmonic of the  $^1\text{H}$  ENDOR signals (cf. Figure 5). Parameters: inversion pulse = 80 ns,  $\pi/2$  pulse = 12 ns,  $\tau$  = 300 ns, and RF length = 30  $\mu\text{s}$ . Simulation:  $g = [1.967, 1.899, 1.788]$ ,  $A^{27}\text{Al} = [22, 45, 35]$  MHz, Euler angle =  $[35, 35, -35]^\circ$ , and  $P = [-0.5, 1.0, -0.5]$  MHz, where  $P$  is coaxial with  $A$ .

higher-order RF harmonic signals (Figure S8) and, therefore, are not used for data interpretation.

The field-dependent ENDOR spectra are simulated using  $A^{27}\text{Al} = [22, 45, 35]$  MHz. The magnitude of this HFI is reasonably similar to that from DFT calculation ( $A_{\text{DFT}}^{27}\text{Al} = [29.0, 29.9, 37.5]$  MHz; Table S2) although the dipolar part seems to be underestimated. While no quadrupole features are resolved in the ENDOR spectra, the maximum breadth of the  $^{27}\text{Al}$  features (obtained at fields near  $g_2$ ) allows estimation of the NQI tensor as  $\sim [-0.5, 1.0, -0.5]$  MHz, in a magnitude similar to that of the Ti complex; the asymmetry parameter is not estimated. Decomposition of  $A$  gives  $a_{\text{iso}}^{27}\text{Al} = 34$  MHz and the dipolar part of  $T_{\text{dip}} = [-12, 11, 1]$  MHz. The isotropic hyperfine coupling corresponds to an Al 3s spin density of 0.9%. The dipolar part can be analyzed similar to the case of **1a** (vide supra; see the SI), yielding a  $T_{\text{loc}} = [-11.4, 9.8, 1.6]$  MHz and a 3p spin density of 14%. As one can tell, in the case of **2**, the major contribution to  $T_{\text{dip}}$  is the local component, caused by a much larger spin density on the Al 3p orbitals. The total spin density on the Al is therefore estimated to be  $\sim 15\%$  with the 3s contribution included. This substantial spin delocalization is consistent with the calculation results that give a Mayer bond order of 0.7 between Th and Al (see the SI).

## DISCUSSION

**Electronic Structural Origins of  $g$  Values.** In order to understand the electronic structures of these two complexes and how they are affected by the Alanate ligand, we started to build a qualitative MO diagram for the two complexes (Figure 7). The MOs for bent metallocenes have been well-described by Lauher and Hoffmann<sup>47</sup> and are shown in Figure 7 using the coordination system in our study. The MOs of complexes **1a/1b** and **2** are adapted from those of Cp<sub>2</sub>Nb(BH<sub>4</sub>), which has a double-bridged structure, and Cp<sub>2</sub>Sc(BH<sub>4</sub>) with a triple-bridged structure, respectively.<sup>65</sup> In both cases, the alanate ligand donates a total of four electrons to the Cp<sub>2</sub>M<sup>+</sup> moiety, resulting in a 17e<sup>−</sup> system. The unpaired electron occupies the low-lying metal-based 1a<sub>1</sub> orbital ( $d_z^2$  mixed with some  $d_{x^2-y^2}$ ), which is essentially nonbonding and interacts only weakly with the ligands. The LUMO, b<sub>2</sub>, has mainly  $d_{yz}$  character and forms a  $\pi$ -type bond with one of the alanate orbitals derived from the t<sub>2</sub> orbital quantized along the M–Al axis. The 2a<sub>1</sub> orbital, with  $d_{x^2-y^2}$  character, forms a  $\sigma$  bond with another t<sub>2</sub> orbital, leaving the third t<sub>2</sub> orbital nonbonding.

Deviation of the  $g$  values from  $g_e$  in transition-metal complexes is due to spin–orbit couplings that mix the excited states into the ground states. For bent metallocenes, Peterson and Dahl have shown that the  $g$  values can be formulated as follows:<sup>44,66,67</sup>

$$g_x = g_e - \frac{2\lambda k_x^2 (\sqrt{3}a + b)^2}{\Delta E_{yz}}; \quad g_y = g_e - \frac{2\lambda k_y^2 (\sqrt{3}a - b)^2}{\Delta E_{xz}}; \quad g_z = g_e - \frac{8\lambda k_z^2 b^2}{\Delta E_{xy}} \quad (1)$$

where  $\lambda$  is the atomic spin–orbital coupling constant,  $\Delta E_{yz}$ ,  $\Delta E_{xz}$ , and  $\Delta E_{xy}$  are the energies (relative to the ground state) of the excited states of  $d_{yz}$ ,  $d_{xz}$ , and  $d_{xy}$  character (that is, the b<sub>2</sub>, 2a<sub>1</sub>, and b<sub>1</sub> orbitals, respectively),  $a$  and  $b$  are the coefficients of  $d_z^2$  and  $d_{x^2-y^2}$  in the ground state, and  $k_{x,y,z}$  are the orbital



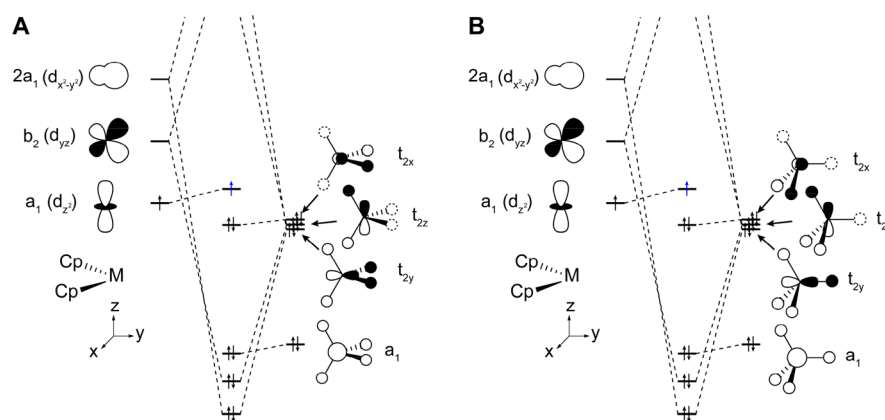


**Figure 7.** Qualitative MO diagrams for double- and triple-bridged  $\text{Cp}_2\text{M}^+$  complexes with  $d^1$  configuration. SOMO electrons are shown in blue. Metal f orbitals are not included.

reduction factors accounting for the d character (covalency) in each MO.

For the Ti complex, because  $g_z$  ( $g_1 = 2.003$ ) is quite close to  $g_e$ , we assume  $b \sim 0$ ; that being said, the  $1a_1$  ground state is almost pure  $3d_{z^2}$ . The small  $g$  shifts of  $g_x$  and  $g_y$  are consistent with the small  $\lambda$  ( $\text{Ti}^{3+}$ ) of  $155 \text{ cm}^{-1}$ . The  $g$  shifts of **1a** are even smaller than all other  $\text{Cp}_2\text{TiX}$  ( $X = \text{F}, \text{Cl}, \text{Br}, \text{OR}, \text{NHR}, \dots$ ) compounds due to the stronger  $\pi$ -type bonding between the metal  $b_2$  ( $d_{yz}$ ) orbital and alanate  $t_2$  orbital, which destabilizes the former, leading to a larger  $\Delta E_{yz}$ .<sup>67</sup>

For the Th complex, the  $g$  values and line shape of the EPR spectrum indicate that the contribution of the f orbital to the ground state is negligible. The much larger separation of principal  $g$  values and deviations from  $g_e$  compared to that of the Ti complex indicate the much larger spin–orbit coupling of  $\text{Th}^{3+}$ . However, simply extrapolating these MO descriptions established for the 3d elements is less quantitatively informative, and employing this first-order perturbation theory approach for the quantitative analysis of  $g$  values may not apply to complexes of much heavier ions.<sup>68</sup> Furthermore, the ligand-field splittings are unknown because the electronic spectrum of **2** is dominated by the electric-dipole-allowed  $6d \rightarrow 5f$  transitions,<sup>25</sup> obscuring the Laporte-forbidden  $d \rightarrow d$  transitions.<sup>25</sup> Instead, we compare the  $g$  values of **2** to those of other  $\text{Th}^{3+}$  systems (Table S3). The more symmetric molecule  $(\text{Cp}^t)_3\text{Th}$  has an axial  $\mathbf{g} = [1.974, 1.880, 1.880]$ .<sup>23</sup> The axiality of this  $\mathbf{g}$  tensor is caused by the pseudo- $C_{3h}$  ligand field that splits the d orbitals into the ground state  $A'$  ( $d_{z^2}$ ), the doubly degenerate  $E''$  ( $d_{xz}$  and  $d_{yz}$ ), and the doubly degenerate  $E'$  ( $d_{x^2-y^2}$  and  $d_{xy}$ ), leading to equal  $\Delta E_{yz}$  and  $\Delta E_{xz}$ . In this scenario, the direction of  $g_z$  can be naturally assigned as the  $C_3$  axis of the molecule. In complex **2**, one of the Cp ligands is replaced by the alanate moiety, which removes the  $C_3$  axis, the degeneracy of  $d_{xz}$  and  $d_{yz}$  and, with that, the axiality of the  $\mathbf{g}$  tensor. Interestingly, the value of  $g_1$  is almost unaffected, suggesting that the direction of  $g_z$  may be unaltered. The presence of the alanate ligand causes a large shift of  $g_3$  from 1.880 to 1.788 ( $g_e - g_y = 0.12\text{--}0.21$ ), indicating a significantly decreased  $\Delta E_{yz}$  as indicated from eq 1. Similar  $g$  shifts have been observed in another bimetallic  $\text{Th}^{3+}$  complex,  $\text{Cp}_2\text{ThH}_3\text{ThHCp}_2$ , with  $\mathbf{g} = [1.98, 1.94, 1.76]$ , in which three hydrides bridge the  $\text{Th}^{3+}$  center to a  $\text{Th}^{4+}$  center; however, unlike our  $\text{Al}^{3+}$  system, DFT calculations suggested that no spin density is delocalized in this  $\text{Th}^{4+}$  center.<sup>69</sup>

**M–Al Bonding in 1a and 2.** The differences in the  $^1\text{H}$  and  $^{27}\text{Al}$  ENDOR results of **1a** and **2** allow us to compare the bonding pictures between them. The bridging hydrides in **1a** and **2** have similar  $a_{\text{iso}}$  values; both are negative and relatively small, caused by the small overlap between the nonbonding  $d_{z^2}$  orbital and the hydride's  $1s$  orbital. The much larger rhombicity of  $^1\text{H}$  HFI in **2** reflects the diffuse nature of  $6d_{z^2}$  compared to  $3d_{z^2}$ , as expected. In contrast, the spin density on Al in **2** is  $\sim 5$ -fold larger than that in **1a**, suggesting a significant overlap between the  $\text{Th}^{3+}$  SOMO and the Al 3p orbitals. Our previous DFT calculation suggested that the spin density is transferred from the Th 6d-based orbital to an antibonding Al-CTMS<sub>3</sub> orbital with significant Al 3p character, and no such interaction is present in the  $\text{Ti}^{3+}$  complex. The presence of this interaction suggests that Al acts as an electron acceptor to partially stabilize the highly reducing  $\text{Th}^{3+}$ . The polarity of this interaction is supported by a recently reported electronegativity scale that includes the values for Th and Al.<sup>70</sup> More importantly, the large  $a_{\text{iso}}$  values and spin density on Al in **2** further suggest a significant covalency between Th and Al that is missing in the case of **1a**. There are only a handful of  $^{27}\text{Al}$  HFIs reported in molecular systems, and  $^{27}\text{Al}$   $a_{\text{iso}}$  values with magnitudes of 20–30 MHz are only found when Al is directly bound to C radical centers.<sup>41,42,71</sup>

While it is challenging to contextualize this type of metal–metal interaction and examples from transition-metal complexes could differ significantly from those from actinide complexes, a few covalent metal–metal bonds have been suggested in such bridging complexes that may help to understand the Th–Al interaction. The reaction between  $\text{Cp}^*(\text{PMe}_3)\text{Ir}(\text{H}_2)$  and  $\text{Ph}_3\text{Al}$  leads to an bridging hydride adduct,  $\text{Cp}^*(\text{PMe}_3)\text{IrH}_2\text{AlPh}_3$  ( $\text{Cp}^* = \eta^5\text{-pentamethylcyclopentadienyl}$ ), which is believed to contain a Ir–Al bond bridged by the hydrides.<sup>72</sup> In the light-induced Ni–L state of the [NiFe] hydrogenase, the presence of a metal–metal bond between a Ni center and a low-spin  $\text{Fe}^{2+}$  center has been proposed in a quantum-chemical study,<sup>73</sup> which suggested a Ni–Fe Mayer bond order of  $\sim 0.4$  and a spin density on the  $\text{Fe}^{2+}$  center of  $\sim -0.07$ . In this regard, the Th–Al Mayer bond order of 0.7 and the Al spin density of 0.15 in **2** are indeed indications of significant Th–Al metal–metal bonding character. In comparison, the Ti–Al Mayer bond index in **1a** is computed to be merely 0.13, which, together with our ENDOR results, exemplifies the differences of 3d and 6d orbitals in forming such unconventional bonding interactions.

## CONCLUSION

In conclusion, we have characterized by advanced EPR techniques a  $\text{Th}^{3+}$  complex and a  $\text{Ti}^{3+}$  analogue, both containing M–H–Al bridges, in order to extract the  $^1\text{H}$  and  $^{27}\text{Al}$  hyperfine parameters. We further used these parameters to calculate the spin-density distributions in these complexes and to analyze the differences between the M–H and M–Al bonding interactions. Our results indicate that the  $^1\text{H}$  HFIs of the bridging hydrides are similar in both complexes and can be explained by using a model of spin polarization by the half-occupied  $d_z^2$ . In contrast, we observed a more dramatic difference in the  $^{27}\text{Al}$  HFI between these two complexes, calculated to originate from  $\sim 5$  times more spin density on Al in the Th complex. The hyperfine parameters of H and Al in these two complexes indicate direct orbital overlap between Th and Al in the Th complex, leading to significant covalent bonding between them. Our study provides a model for actinide bonding that is a useful reference for studying similar compounds that could have unusual properties and applications.

## ASSOCIATED CONTENT

### Supporting Information

The Supporting Information is available free of charge on the ACS Publications website at DOI: 10.1021/acs.inorgchem.9b00720.

Summary of the calculation results, additional EPR and ENDOR spectra, notes for the three-point-dipole model, and analyses of the  $^{27}\text{Al}$  HFI and NQI parameters (PDF)

## AUTHOR INFORMATION

### Corresponding Authors

\*E-mail: arnold@berkeley.edu.

\*E-mail: rdbritt@ucdavis.edu.

### ORCID

Guodong Rao: 0000-0001-8043-3436

Lizhi Tao: 0000-0001-9921-2297

Troy A. Stich: 0000-0003-0710-1456

John Arnold: 0000-0001-9671-227X

R. David Britt: 0000-0003-0889-8436

### Present Address

<sup>†</sup>T.A.S.: Department of Chemistry, Wake Forest University, Winston-Salem, NC 27101.

### Notes

The authors declare no competing financial interest.

## ACKNOWLEDGMENTS

This work was funded by the National Institute of Health (Grant 1R35GM126961-01 to R.D.B.). Synthetic aspects of the work were supported by the Director, Office of Science, Office of Basic Energy Sciences, Division of Chemical Sciences, Geosciences, and Biosciences Heavy Element Chemistry Program of the U.S. Department of Energy at Lawrence Berkeley National Laboratory under Contract DE-AC02-05CH11231.

## REFERENCES

- (1) Ewing, R. C. Long-term storage of spent nuclear fuel. *Nat. Mater.* **2015**, *14*, 252–7.
- (2) Kaltsoyannis, N. Does covalency increase or decrease across the actinide series? Implications for minor actinide partitioning. *Inorg. Chem.* **2013**, *52*, 3407–13.
- (3) Bünzli, J.-C. G. Review: Lanthanide coordination chemistry: from old concepts to coordination polymers. *J. Coord. Chem.* **2014**, *67*, 3706–3733.
- (4) Kaltsoyannis, N.; Hay, P. J.; Li, J.; Blaudau, J. P.; Bursten, B. E. Theoretical studies of the electronic structure of compounds of the actinide elements. In *The Chemistry of the Actinide and Transactinide Elements*, 3rd ed.; Morss, L. R., Edelstein, N. M., Fuger, J., Katz, J. J., Eds.; Springer: Dordrecht, The Netherlands, 2006; pp 1893–2012.
- (5) Neidig, M. L.; Clark, D. L.; Martin, R. L. Covalency in f-element complexes. *Coord. Chem. Rev.* **2013**, *257*, 394–406.
- (6) Ball, P. Beyond the bond. *Nature* **2011**, *469*, 26–8.
- (7) Cantat, T.; Graves, C. R.; Jantunen, K. C.; Burns, C. J.; Scott, B. L.; Schelter, E. J.; Morris, D. E.; Hay, P. J.; Kiplinger, J. L. Evidence for the involvement of 5f orbitals in the bonding and reactivity of organometallic actinide compounds: thorium(IV) and uranium(IV) bis(hydrazonato) complexes. *J. Am. Chem. Soc.* **2008**, *130*, 17537–51.
- (8) Gardner, B. M.; Cleaves, P. A.; Kefalidis, C. E.; Fang, J.; Maron, L.; Lewis, W.; Blake, A. J.; Liddle, S. T. The role of 5f-orbital participation in unexpected inversion of the  $\sigma$ -bond metathesis reactivity trend of triamidoamine thorium(IV) and uranium(IV) alkyls. *Chem. Sci.* **2014**, *5*, 2489–2497.
- (9) Jantunen, K. C.; Scott, B. L.; Kiplinger, J. L. A comparative study of the reactivity of Zr(IV), Hf(IV) and Th(IV) metallocene complexes: Thorium is not a Group IV metal after all. *J. Alloys Compd.* **2007**, *444–445*, 363–368.
- (10) Minasian, S. G.; Keith, J. M.; Batista, E. R.; Boland, K. S.; Clark, D. L.; Conradson, S. D.; Kozimor, S. A.; Martin, R. L.; Schwarz, D. E.; Shuh, D. K.; Wagner, G. L.; Wilkerson, M. P.; Wolfsberg, L. E.; Yang, P. Determining relative f and d orbital contributions to M–Cl covalency in  $\text{MCl}_6^{2-}$  (M = Ti, Zr, Hf, U) and  $\text{UOCl}_5^-$  using Cl K-edge X-ray absorption spectroscopy and time-dependent density functional theory. *J. Am. Chem. Soc.* **2012**, *134*, 5586–97.
- (11) Pepper, M.; Bursten, B. E. The electronic structure of actinide-containing molecules: a challenge to applied quantum chemistry. *Chem. Rev.* **1991**, *91*, 719–741.
- (12) Denning, R. G. Electronic structure and bonding in actinyl ions and their analogs. *J. Phys. Chem. A* **2007**, *111*, 4125–43.
- (13) Kerridge, A.; Kaltsoyannis, N. Are the ground states of the later actinocenes multiconfigurational? All-electron spin-orbit coupled CASPT2 calculations on  $\text{An}(\eta^8\text{-C}_8\text{H}_8)_2$  (An = Th, U, Pu, Cm). *J. Phys. Chem. A* **2009**, *113*, 8737–45.
- (14) Brennan, J. G.; Green, J. C.; Redfern, C. M. Covalency in bis([8]annulene)uranium from photoelectron spectroscopy with variable photon energy. *J. Am. Chem. Soc.* **1989**, *111*, 2373–2377.
- (15) Solomon, E. I.; Hedman, B.; Hodgson, K. O.; Dey, A.; Szilagyi, R. K. Ligand K-edge X-ray absorption spectroscopy: covalency of ligand–metal bonds. *Coord. Chem. Rev.* **2005**, *249*, 97–129.
- (16) Hüfner, S. *Photoelectron Spectroscopy Principles and Applications*; Springer: New York, 2003.
- (17) Goodman, B. A.; Raynor, J. B. Electron spin resonance of transition metal complexes. In *Advances in Inorganic Chemistry and Radiochemistry*; Emeléus, H. J., Sharpe, A. G., Eds.; Academic Press, 1970; Vol. 13, pp 135–362.
- (18) Kalvius, G. M. Mössbauer spectroscopy of actinides: Some applications to solid state chemistry. *J. Less-Common Met.* **1986**, *121*, 353–378.
- (19) Clark, J. P.; Green, J. C. An investigation of the electronic structure of bis( $\eta$ -cyclo-octatetraene)-actinoids by helium-(I) and -(II) photoelectron spectroscopy. *J. Chem. Soc., Dalton Trans.* **1977**, *0*, 505–508.
- (20) Kozimor, S. A.; Yang, P.; Batista, E. R.; Boland, K. S.; Burns, C. J.; Clark, D. L.; Conradson, S. D.; Martin, R. L.; Wilkerson, M. P.; Wolfsberg, L. E. Trends in covalency for d- and f-element metallocene dichlorides identified using chlorine K-edge X-ray absorption spectroscopy and time-dependent density functional theory. *J. Am. Chem. Soc.* **2009**, *131*, 12125–36.

- (21) Kolbe, W.; Edelstein, N. Electron-nuclear double resonance of  $\text{Pu}^{3+}$  in  $\text{CaF}_2$ . *Phys. Rev. B* **1971**, *4*, 2869–2875.
- (22) Kot, W. K.; Shalimoff, G. V.; Edelstein, N. M.; Edelman, M. A.; Lappert, M. F.  $[\text{Th}(\text{III})[\eta^5\text{-C}_5\text{H}_5(\text{SiMe}_3)_2]_3]$ , an actinide compound with a  $6d^1$  ground state. *J. Am. Chem. Soc.* **1988**, *110*, 986–987.
- (23) Formanuk, A.; Ariciu, A. M.; Ortu, F.; Beekmeyer, R.; Kerridge, A.; Tuna, F.; McInnes, E. J. L.; Mills, D. P. Actinide covalency measured by pulsed electron paramagnetic resonance spectroscopy. *Nat. Chem.* **2017**, *9*, 578–583.
- (24) Brown, A. C.; Altman, A. B.; Lohrey, T. D.; Hohloch, S.; Arnold, J. Hydride oxidation from a titanium-aluminum bimetallic complex: insertion, thermal and electrochemical reactivity. *Chem. Sci.* **2017**, *8*, 5153–5160.
- (25) Altman, A. B.; Brown, A. C.; Rao, G.; Lohrey, T. D.; Britt, R. D.; Maron, L.; Minasian, S. G.; Shuh, D. K.; Arnold, J. Chemical structure and bonding in a thorium(III)-aluminum heterobimetallic complex. *Chem. Sci.* **2018**, *9*, 4317–4324.
- (26) Raleigh, D. Prepare thorium-aluminum alloys by direct reduction. *Ind. Eng. Chem.* **1961**, *53*, 445–448.
- (27) *The Chemistry of the Actinide and Transactinide Elements*; Springer: Dordrecht, The Netherlands, 2006.
- (28) Calvo, R.; Abresch, E. C.; Bittl, R.; Feher, G.; Hofbauer, W.; Isaacson, R. A.; Lubitz, W.; Okamura, M. Y.; Paddock, M. L. EPR study of the molecular and electronic structure of the semiquinone biradical  $\text{Q}(\text{A})\cdot\text{Q}(\text{B})\cdot$  in photosynthetic reaction centers from *Rhodospirillum rubrum*. *J. Am. Chem. Soc.* **2000**, *122*, 7327–7341.
- (29) Stoll, S.; Schweiger, A. EasySpin, a comprehensive software package for spectral simulation and analysis in EPR. *J. Magn. Reson.* **2006**, *178*, 42–55.
- (30) Schweiger, A.; Jeschke, G. *Principles of Pulse Electron Paramagnetic Resonance*; Oxford University Press: New York, 2001.
- (31) Neese, F. The ORCA program system. *Wiley Interdisciplinary Reviews: Computational Molecular Science* **2012**, *2*, 73–78.
- (32) Staroverov, V. N.; Scuseria, G. E.; Tao, J.; Perdew, J. P. Comparative assessment of a new nonempirical density functional: Molecules and hydrogen-bonded complexes. *J. Chem. Phys.* **2003**, *119*, 12129–12137.
- (33) Neese, F.; Wennmohs, F.; Hansen, A.; Becker, U. Efficient, approximate and parallel Hartree–Fock and hybrid DFT calculations. A ‘chain-of-spheres’ algorithm for the Hartree–Fock exchange. *Chem. Phys.* **2009**, *356*, 98–109.
- (34) Weigend, F. Accurate coulomb-fitting basis sets for H to Rn. *Phys. Chem. Chem. Phys.* **2006**, *8*, 1057–1065.
- (35) Pantazis, D. A.; Neese, F. All-electron scalar relativistic basis sets for the lanthanides. *J. Chem. Theory Comput.* **2009**, *5*, 2229–38.
- (36) Pantazis, D. A.; Chen, X. Y.; Landis, C. R.; Neese, F. All-electron scalar relativistic basis sets for third-row transition metal atoms. *J. Chem. Theory Comput.* **2008**, *4*, 908–19.
- (37) Pantazis, D. A.; Neese, F. All-electron scalar relativistic basis sets for the 6p elements. *Theor. Chem. Acc.* **2012**, *131*, 1292.
- (38) Pantazis, D. A.; Neese, F. All-electron scalar relativistic basis sets for the actinides. *J. Chem. Theory Comput.* **2011**, *7*, 677–684.
- (39) In the simulation of CW EPR using the *Easyspin* toolbox, only  $a_{\text{iso}}$  of  $^{47}\text{Ti}$  is required in the input and all of the isotopes of Ti are automatically considered by scaling  $a_{\text{iso}}$  according to the gyromagnetic ratios of the other nuclei.
- (40) Mile, B.; Howard, J. A.; Tse, J. S. EPR studies of the addition of aluminum and gallium atoms to allene: a rule for regioselectivity. *Organometallics* **1988**, *7*, 1278–1282.
- (41) Dohmeier, C.; Mocker, M.; Schnöckel, H.; Lötze, A.; Schneider, U.; Ahlrichs, R.  $[\text{Al}(\text{Bu})_6]^-$ : EPR spectroscopic evidence and ab initio calculations. *Angew. Chem., Int. Ed. Engl.* **1993**, *32*, 1428–1430.
- (42) Kundu, S.; Sinhababu, S.; Dutta, S.; Mondal, T.; Koley, D.; Dittrich, B.; Schwederski, B.; Kaim, W.; Stuckl, A. C.; Roesky, H. W. Synthesis and characterization of Lewis base stabilized mono- and di-organo aluminum radicals. *Chem. Commun. (Cambridge, U. K.)* **2017**, *53*, 10516–10519.
- (43) Waters, E. L.; Maki, A. H.  $\text{Ti}^{47}$  and  $\text{Ti}^{49}$  hyperfine structure in the electron spin resonance of titanium (III) complexes. *Phys. Rev.* **1962**, *125*, 233–234.
- (44) Petersen, J. L.; Dahl, L. F. Synthesis and structural characterization by X-ray diffraction and EPR single-crystal techniques of (dichloro)bis( $\eta^5$ -methylcyclopentadienyl)vanadium and (dichloro)bis( $\eta^5$ -methylcyclopentadienyl)titanium. Spatial distribution of the unpaired electron in a  $V(\eta^5\text{-C}_5\text{H}_5)_2\text{L}_2$ -type complex. *J. Am. Chem. Soc.* **1975**, *97*, 6422–6433.
- (45) Petersen, J. L.; Lichtenberger, D. L.; Fenske, R. F.; Dahl, L. F. Nonparameterized molecular orbital calculations and photoelectron spectroscopy of open- and closed-shell  $\text{M}(\text{IV}) \text{M}(\eta^5\text{-C}_5\text{H}_5)_2\text{L}_2$  complexes. *J. Am. Chem. Soc.* **1975**, *97*, 6433–6441.
- (46) Francesconi, L. C.; Corbin, D. R.; Clauss, A. W.; Hendrickson, D. N.; Stucky, G. D. Binuclear dicyclopentadienyltitanium(III) complexes: magnetic exchange interactions propagated by the methylene groups of aliphatic dicarboxylic acid dianions. *Inorg. Chem.* **1981**, *20*, 2059–2069.
- (47) Lauher, J. W.; Hoffmann, R. Structure and chemistry of bis(cyclopentadienyl)- $\text{ML}_n$  complexes. *J. Am. Chem. Soc.* **1976**, *98*, 1729–1742.
- (48) Kinney, R. A.; Saouma, C. T.; Peters, J. C.; Hoffman, B. M. Modeling the signatures of hydrides in metalloenzymes: ENDOR analysis of a Di-iron  $\text{Fe}(\mu\text{-NH})(\mu\text{-H})\text{Fe}$  core. *J. Am. Chem. Soc.* **2012**, *134*, 12637–47.
- (49) Gu, N. X.; Oyala, P. H.; Peters, J. C. An  $S = 1/2$  iron complex featuring  $\text{N}_2$ , thiolate, and hydride ligands: Reductive elimination of  $\text{H}_2$  and relevant thermochemical Fe–H parameters. *J. Am. Chem. Soc.* **2018**, *140*, 6374–6382.
- (50) Igarashi, R. Y.; Laryukhin, M.; Dos Santos, P. C.; Lee, H. I.; Dean, D. R.; Seefeldt, L. C.; Hoffman, B. M. Trapping  $\text{H}^-$  bound to the nitrogenase FeMo-cofactor active site during  $\text{H}_2$  evolution: characterization by ENDOR spectroscopy. *J. Am. Chem. Soc.* **2005**, *127*, 6231–41.
- (51) Rittle, J.; McCrory, C. C.; Peters, J. C. A  $10^6$ -fold enhancement in  $\text{N}_2$ -binding affinity of an  $\text{Fe}_2(\mu\text{-H})_2$  core upon reduction to a mixed-valence  $\text{Fe}^{\text{II}}\text{Fe}^{\text{I}}$  state. *J. Am. Chem. Soc.* **2014**, *136*, 13853–62.
- (52) Chiang, K. P.; Scarborough, C. C.; Horitani, M.; Lees, N. S.; Ding, K.; Dugan, T. R.; Brennessel, W. W.; Bill, E.; Hoffman, B. M.; Holland, P. L. Characterization of the Fe–H bond in a three-coordinate terminal hydride complex of iron(I). *Angew. Chem., Int. Ed.* **2012**, *51*, 3658–62.
- (53) Brecht, M.; van Gastel, M.; Buhrke, T.; Friedrich, B.; Lubitz, W. Direct detection of a hydrogen ligand in the  $[\text{NiFe}]$  center of the regulatory  $\text{H}_2$ -sensing hydrogenase from *Ralstonia eutropha* in its reduced state by HYSCORE and ENDOR spectroscopy. *J. Am. Chem. Soc.* **2003**, *125*, 13075–83.
- (54) Gunderson, W. A.; Suess, D. L.; Fong, H.; Wang, X.; Hoffmann, C. M.; Cutsail, G. E., 3rd; Peters, J. C.; Hoffman, B. M. Free  $\text{H}_2$  rotation vs Jahn–Teller constraints in the nonclassical trigonal (TPB) $\text{Co-H}_2$  complex. *J. Am. Chem. Soc.* **2014**, *136*, 14998–5009.
- (55) Morton, J. R.; Preston, K. F. Atomic parameters for paramagnetic resonance data. *J. Magn. Reson.* **1978**, *30*, 577–582.
- (56) Weil, J. A.; Bolton, J. R., Hyperfine (A) anisotropy. *Electron Paramagnetic Resonance*; John Wiley & Sons, Inc., 2006; pp 118–157.
- (57) Stoll, S.; Nejaty-Jahr, Y.; Woodward, J. J.; Ozarowski, A.; Marletta, M. A.; Britt, R. D. Nitric oxide synthase stabilizes the tetrahydrobiopterin cofactor radical by controlling its protonation state. *J. Am. Chem. Soc.* **2010**, *132*, 11812–23.
- (58) This is done in *Matlab*. Briefly, these T tensors are first transformed from their point-dipole frames into the molecular frame, weighed by the spin-density factor, summed, and diagonalized to give the total effective  $T_{\text{cal}}$ .
- (59) Munzarová, M. L.; Kubáček, P.; Kaupp, M. Mechanisms of epr hyperfine coupling in transition metal complexes. *J. Am. Chem. Soc.* **2000**, *122*, 11900–11913.
- (60) Gerson, F.; Huber, W., Spin density, spin population, spin polarization, and spin delocalization. *Electron Spin Resonance Spectroscopy of Organic Radicals*; Wiley-VCH, 2003; pp 61–64.



- (61) Terhune, R. W.; Lambe, J.; Makhov, G.; Cross, L. G. Electron nuclear double resonance experiments with ruby. *Phys. Rev. Lett.* **1960**, *4*, 234–236.
- (62) Carl, P. J.; Vaughan, D. E.; Goldfarb, D. High field  $^{27}\text{Al}$  ENDOR reveals the coordination mode of  $\text{Cu}^{2+}$  in low Si/Al zeolites. *J. Am. Chem. Soc.* **2006**, *128*, 7160–1.
- (63) Azamat, D. V.; Badalyan, A. G.; Feng, D. H.; Lančok, J.; Jastrabik, L.; Dejneka, A.; Baranov, P. G.; Yakovlev, D. R.; Bayer, M. ENDOR investigations of the  $\text{Ce}^{3+}$  ions in YAG: Transferred hyperfine interaction with nearest aluminum ions. *J. Appl. Phys.* **2017**, *122*, 243903.
- (64) Cutsail, G. E., 3rd; Stein, B. W.; Subedi, D.; Smith, J. M.; Kirk, M. L.; Hoffman, B. M. EPR, ENDOR, and electronic structure studies of the Jahn-Teller distortion in an  $\text{Fe(V)}$  nitride. *J. Am. Chem. Soc.* **2014**, *136*, 12323–36.
- (65) Mancini, M.; Bougeard, P.; Burns, R. C.; Mlekuz, M.; Sayer, B. G.; Thompson, J. I. A.; McGlinchey, M. J. Bonding in transition-metal tetrahydroborates: a multinuclear magnetic resonance study of  $(\text{C}_5\text{H}_5)_2\text{Sc}(\text{BH}_4)$  and  $\text{Sc}(\text{BH}_4)_3$  and some comments on the isolobality of  $\text{BH}_4^-$ , halide, and  $\eta^5\text{-C}_5\text{H}_5^-$  groups. *Inorg. Chem.* **1984**, *23*, 1072–1078.
- (66) Petersen, J. L.; Dahl, L. F. Dilute single-crystal electron paramagnetic resonance study of bis(cyclopentadienyl)vanadium pentasulfide,  $\text{V}(\eta^5\text{-C}_5\text{H}_5)_2\text{S}_5$ . Coup de grace to the Ballhausen-Dahl bonding model applied to  $\text{M}(\eta^5\text{-C}_5\text{H}_5)_2\text{L}_2$ -type complexes. *J. Am. Chem. Soc.* **1975**, *97*, 6416–6422.
- (67) Lukens, W. W.; Smith, M. R.; Andersen, R. A. A  $\pi$ -donor spectrochemical series for x in  $(\text{Me}_5\text{C}_5)_2\text{TiX}$ , and  $\beta$ -agostic interactions in  $\text{X} = \text{Et}$  and  $\text{N}(\text{Me})\text{Ph}$ . *J. Am. Chem. Soc.* **1996**, *118*, 1719–1728.
- (68) King, D. M.; Cleaves, P. A.; Wooles, A. J.; Gardner, B. M.; Chilton, N. F.; Tuna, F.; Lewis, W.; McInnes, E. J.; Liddle, S. T. Molecular and electronic structure of terminal and alkali metal-capped uranium(V) nitride complexes. *Nat. Commun.* **2016**, *7*, 13773.
- (69) Langeslay, R. R.; Fieser, M. E.; Ziller, J. W.; Furche, F.; Evans, W. J. Expanding thorium hydride chemistry through  $\text{Th}^{2+}$ , including the synthesis of a mixed-valent  $\text{Th}^{4+}/\text{Th}^{3+}$  hydride complex. *J. Am. Chem. Soc.* **2016**, *138*, 4036–45.
- (70) Rahm, M.; Zeng, T.; Hoffmann, R. Electronegativity seen as the ground state average valence electron binding energy. *J. Am. Chem. Soc.* **2019**, *141*, 342–51.
- (71) Li, B.; Kundu, S.; Stuckl, A. C.; Zhu, H.; Keil, H.; Herbst-Irmer, R.; Stalke, D.; Schwederski, B.; Kaim, W.; Andrada, D. M.; Frenking, G.; Roesky, H. W. A stable neutral radical in the coordination sphere of aluminum. *Angew. Chem., Int. Ed.* **2017**, *56*, 397–400.
- (72) Golden, J. T.; Peterson, T. H.; Holland, P. L.; Bergman, R. G.; Andersen, R. A. Adduct formation and single and double deprotonation of  $\text{Cp}^*(\text{PMe}_3)\text{Ir}(\text{H})_2$  with main group metal alkyls and aryls: Synthesis and structure of three novel Ir-Al and Ir-Mg heterobimetallics. *J. Am. Chem. Soc.* **1998**, *120*, 223–224.
- (73) Kampa, M.; Pandelia, M. E.; Lubitz, W.; van Gestel, M.; Neese, F. A metal-metal bond in the light-induced state of  $[\text{NiFe}]$  hydrogenases with relevance to hydrogen evolution. *J. Am. Chem. Soc.* **2013**, *135*, 3915–25.